Folding energy landscape of cytochrome cb_{562}

Tetsunari Kimura, Jennifer C. Lee[1], Harry B. Gray[2], and Jay R. Winkler[2]

Beckman Institute, California Institute of Technology, Pasadena, CA 91125-7400

Contributed by Harry B. Gray, March 9, 2009 (sent for review February 11, 2009)

Cytochrome cb_{562} is a variant of an *Escherichia coli* four-helix bundle *b*-type heme protein in which the porphyrin prosthetic group is covalently ligated to the polypeptide near the terminus of helix 4. Studies from other laboratories have shown that the apoprotein folds rapidly without the formation of intermediates, whereas the holoprotein loses heme before native structure can be attained. Time-resolved fluorescence energy transfer (TRFET) measurements of cytochrome cb_{562} refolding triggered using an ultrafast continuous-flow mixer (150 μs dead time) reveal that heme attachment to the polypeptide does not interfere with rapid formation of the native structure. Analyses of the TRFET data produce distributions of Trp-59–heme distances in the protein before, during, and after refolding. Characterization of the moments and time evolution of these distributions provides compelling evidence for a refolding mechanism that does not involve significant populations of intermediates. These observations suggest that the cytochrome b_{562} folding energy landscape is minimally frustrated and able to tolerate the introduction of substantial perturbations (i.e., the heme prosthetic group) without the formation of deep misfolded traps.

four-helix bundle | minimal frustration | protein folding | time-resolved fluorescence energy transfer | tryptophan

Energy landscape theory has delineated principles that underlie the conversion of disordered polypeptides into correctly folded functional proteins (1–8). A key element of this theory is the concept of minimal frustration that, in its qualitative formulation, predicts that the folding energy landscape is funneled toward the native structure and does not contain a large number of deep misfolded traps. This notion derives in part from the many experimental observations of proteins that rapidly fold to native structures without the apparent population of intermediates. Additional features of minimal frustration are the robustness of protein structures to mutation and the malleability of folding pathways (1, 3–5, 7).

The incorporation of prosthetic groups into protein structures introduces additional challenges for understanding folding and the maintenance of minimally frustrated folding pathways. The heme cofactors in *b*- and *c*-type cytochromes are a case in point. The apoprotein of mitochondrial cytochrome *c* (cyt *c*) is unstructured, demonstrating that heme is required to stabilize the native fold (9). The covalently bound porphyrin plays an integral role in cyt *c* folding, possibly as a hydrophobic nucleation site, but does not lead to nonnative clusters and misfolded traps (10). Many *b*-type cytochromes (e.g., cyt b_5 and cyt b_{562}), however, adopt native or near-native structures in the absence of their noncovalently bound porphyrins (11–23). On the basis of these observations, it has been suggested that folding precedes heme incorporation in the *b*-type cytochromes, whereas heme attachment is a prerequisite for folding in the *c*-type proteins. Because *b*-type cytochromes likely evolved to fold in the absence of heme, the conversion of a *b*-type cytochrome into a *c*-type protein might be expected to disrupt the folding landscape of the native protein.

We have examined a family of four-helix bundle cytochromes [cyt b_{562} (24), cyt cb_{562} (25, 26), cyt c_{556} (25), and cyt c' (27–30)] in which refolding times differ by many orders of magnitude despite their strongly conserved structural topology (≈3 Å rmsd) (25, 28, 31–33). In the *b*-type cytochromes (e.g., cyt b_{562}), the heme is attached to the polypeptide only through axial Fe ligation. The kinetics of heme dissociation from the cyt b_{562} polypeptide ($k_{diss} \approx 2–7 \times 10^3$ s^{-1}) compete with refolding dynamics, limiting the yield of the folding reaction in the reduced state and causing irreversible unfolding in the oxidized state (14, 24). To eliminate the complication of heme dissociation, we developed a protocol to overexpress a variant of cyt b_{562} (R98C/Y101C) in which the α-carbons of the protoporphyrin vinyl groups form thioether linkages to two cysteines in a typical CXXCH *c*-type cytochrome-binding motif (e.g., cyt *c*, cyt c_{556}) (26). A K59W mutation, originally introduced to provide a fluorescent probe of folding, proved to increase yields of protein with properly attached hemes. We call this (K59W/R98C/Y101C) cyt b_{562} variant cyt cb_{562}. We found that the presence of two *c*-type thioether linkages does not perturb the wild-type (cyt b_{562}) structure but does have a substantial impact on folding stability. The folding free-energy change for cyt cb_{562}, extrapolated to guanidine hydrochloride [GuHCl] = 0, is -42 ± 4 kJ mol^{-1} (26); this value is substantially greater than that estimated for the wild-type (b_{562}) protein (-30 kJ mol^{-1}) (34) and three times greater than that of the apoprotein (-13 kJ mol^{-1}) (14).

The experimental characterization of conformational heterogeneity and structural changes during protein folding is particularly important to understand the molecular basis of the energy landscape and the detailed sequence of events that accompanies the transformation of an ensemble of denatured proteins into the native state. We have used time-resolved fluorescence energy transfer (TRFET) to estimate the distributions of distances between a fluorescent donor (**D**) and an energy acceptor (**A**) in an ensemble of protein molecules. By performing these measurements during protein folding, the time evolution of the polypeptide ensemble from heterogeneous unfolded to highly homogeneous native states can be determined. Our previous investigations of yeast cyt *c* (35–39) folding revealed the presence of both extended and collapsed conformations in the intermediate states formed within the mixing dead time, providing clear evidence that this protein does not fold by a simple two-state mechanism (U ↔ N).

Owing to the reversibility of cyt cb_{562} denaturation, we were able to probe the kinetics of stopped-flow triggered cyt cb_{562} refolding (26). The heme absorption spectrum reveals that formation of native cyt cb_{562} is biphasic. The rate constant for the faster phase varies with denaturant concentration and has an extrapolated value of 4.2×10^2 s^{-1} at 0 M GuHCl. The rate of the slower phase is independent of denaturant concentration ($k_{obs} \approx 5$ s^{-1}). When refolding is monitored by Trp-59 fluorescence, more than half of the signal amplitude is quenched during

Author contributions: T.K., J.C.L., H.B.G., and J.R.W. designed research; T.K. and J.C.L. performed research; T.K., J.C.L., H.B.G., and J.R.W. analyzed data; and T.K., J.C.L., H.B.G., and J.R.W. wrote the paper.

The authors declare no conflict of interest.

[1]Present address: Laboratory of Molecular Biophysics, National Heart, Lung, and Blood Institute, National Institutes of Health, Bethesda, MD 20892.

[2]To whom correspondence may be addressed. E-mail: hbgray@caltech.edu or winklerj@caltech.edu.

This article contains supporting information online at www.pnas.org/cgi/content/full/0902562106/DCSupplemental.

the stopped-flow mixing dead time (≈5 ms); the residual signal amplitude decays exponentially with a denaturant-dependent rate constant that corresponds to the faster phase observed using heme absorption spectroscopy.

To clarify the missing early stage of the folding reaction, we have used a continuous-flow (CTF) mixer ($\tau_{mixing} < 150$ μs) (40, 41) to trigger the folding reaction. The mixer has been coupled to a picosecond streak camera with a fiberoptic bundle that allows luminescence decays for 25 different folding times to be acquired simultaneously (29). We measured TRFET between a Trp residue (Trp-59) and the heme to monitor refolding of cyt cb_{562}. Analysis of the TRFET data produced distributions of Trp-59–heme center-to-center distances [$P(r_{DA})$] that provide detailed structural insights into the early events in cyt cb_{562} folding.

Results

Moment Analyses. The properties of heterogeneous systems such as denatured proteins are most conveniently described in terms of distribution functions. TRFET measurements provide the data necessary to generate estimated distributions of distances [$P(r_{DA})$] between energy donors and acceptors in a polypeptide ensemble. We characterize these distributions by their moments (see *Methods*) to quantify the average properties and the heterogeneity of the protein under both equilibrium and transient conditions.

GuHCl-Induced Unfolding. We first characterized the equilibrium unfolding transition of cyt cb_{562} by measuring fluorescence energy transfer kinetics between Trp-59 (**D**) and the heme group (**A**). In folded cyt cb_{562} (Fig. 1; 0 M GuHCl), the Trp-59 fluorescence decay kinetics are consistent with a narrow distribution of Trp-59–heme distances centered at 19.4 Å (the center of the distribution is given by the first moment, M_1; see *Methods*), a value that is in good agreement with that determined from the X-ray crystal structure (18.9 Å; Protein Data Bank ID code 2bc5).

More complex behavior is evident after the addition of GuHCl. The Trp-59 fluorescence decay kinetics become slower and nonexponential, and the mean **D–A** distance moves to larger values as [GuHCl] increases (Fig. 1 *A* and *B*). The TRFET kinetics of the denatured protein are indicative of a heterogeneous collection of compact and extended conformations. Near the midpoint of the GuHCl titration ($[GuHCl]_{1/2}$ = 4.2 M), substantial populations of polypeptides in three different **D–A** distance ranges are apparent: shorter distances than folded state ($r_{DA} \leq 16$ Å: ***S*** component), intermediate distances ($22 \leq r_{DA} \leq 30$ Å: ***I*** component) and extended distances ($r_{DA} \geq 30$ Å: ***E*** component). Finally, at GuHCl concentrations >5.5 M, the population of proteins with native **D–A** distances is diminished in favor of ***S*** (≈10%), ***I*** (≈40%), and ***E*** components (≈50%) as shown in Fig. 1*C*. The changes in the populations of all components show cooperative unfolding of cyt cb_{562} with the transition midpoint of 4.2 M and m value of 7.5 kJ mol^{-1} M^{-1}.

The TRFET data do not allow us to say with confidence that the three components identified in the $P(r_{DA})$ distributions represent distinct minima in the energy landscape of the denatured protein. It is possible that the true $P(r_{DA})$ function is a broad, asymmetric single-mode distribution and that the trimodal functions extracted from the fluorescence data are simply a consequence of the uncertainties inherent in the data analysis. Although, the maximum-entropy method used to extract the $P(r_{DA})$ distributions tends to give maximally broadened functions, there is no guarantee that a general single-mode function cannot provide adequate fits to the data. Neither random polymer distribution functions (e.g., freely jointed chain, worm-like chain) nor a simple Gaussian distribution, however, adequately modeled the experimental data (Figs. S1 and S2 and *SI Appendix*).

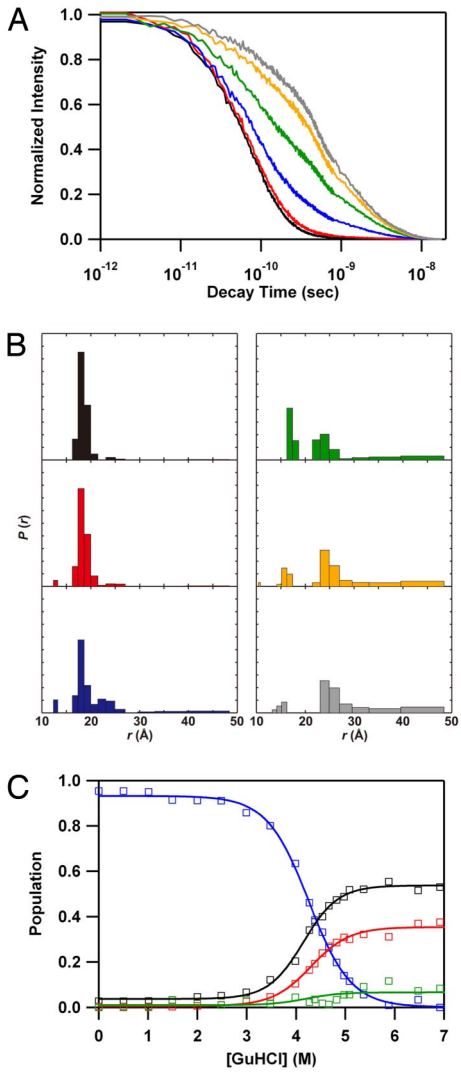

Fig. 1. GuHCl-induced unfolding of cyt cb_{562} (pH 5.0, 50 mM NaOAc) probed by using Trp fluorescence decay. (*A*) Normalized Trp-59 fluorescence decay curves of cyt cb_{562}. For clarity, only 6 of the 19 observed decays are displayed; 0 M (black), 2.0 M (red), 4.0 M (blue), 4.5 M (green), 5.4 M (yellow), and 6.9 M (gray). (*B*) Distributions of Trp-59–heme center-to-center distances [$P(r_{DA})$] extracted from maximum entropy analyses of the TRFET data. The area of each bar reflects the probability amplitude over the corresponding distance range. (*C*) Population changes of each component as a function of the GuHCl concentration (native, blue; short, green; intermediate, red; and extended, black). Solid lines are two-state fitting curves with $[GuHCl]_{1/2}$ = 4.2 M and m = 7.5 kJ mol^{-1} M^{-1}.

Refolding Kinetics. In prior studies using a conventional stopped-flow mixer, we were able to capture only the final stages of cyt cb_{562} refolding. The 150-μs dead time of our CTF mixer provides insights into the early refolding events in this four-helix bundle. The evolution of the Trp-59 fluorescence decay kinetics as the protein refolds (Fig. 2*A*) reveals a gradual transition from the denatured to the folded state. Integration of the individual Trp-59 fluorescence decay traces yields a quantity proportional to the fluorescence quantum yield (Φ_{fl}). Plots of integrated fluorescence intensity as a function of folding time reveal an exponential process with a time constant of ≈4 ms (Fig. 2*B*).

Immediately after the CTF mixing dead time, we observe a

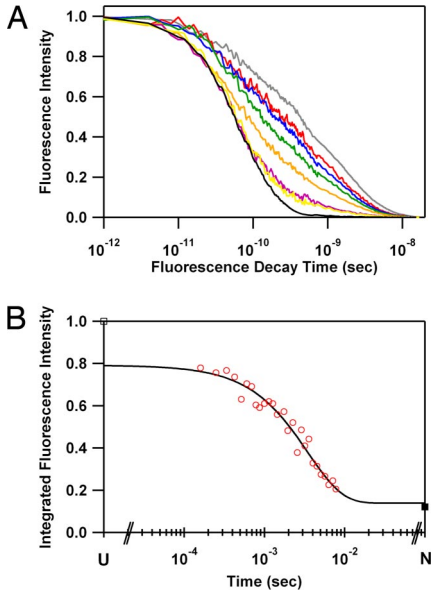

Fig. 2. Folding kinetics of cyt cb_{562} triggered by GuHCl jump from 6.0 M to 1.0 M in a CTF mixer (pH 5.0, 18 °C) probed by Trp-59 fluorescence. (*A*) TRFET data (8 of the 112 measured decays are displayed): 0 (unfolded in 6.0 M GuHCl, gray), 150 μs (red), 430 μs (blue), 1.25 ms (green), 3.41 ms (orange), 6.50 ms (purple), 7.70 ms (yellow), and >30 min (native state in 1.0 M GuHCl, black) after the initiation of folding reaction. (*B*) Integrated Trp-59 fluorescence intensity (Φ_{fl}) as a function of folding time. The 112 original data points are logarithmically smoothed for clarity. Solid line is a fit of the full dataset to a single exponential function with a rate constant of 2.6 ($\pm$0.2) $\times$ 10^2 s^{-1}.

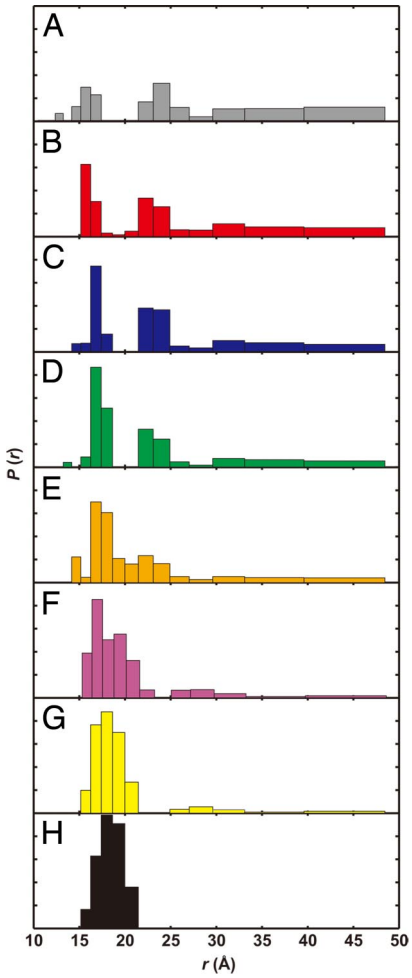

Fig. 3. Distributions of $P(r_{DA})$ for refolding of cyt cb_{562}. The $P(r_{DA})$ distributions are extracted from maximum entropy analyses of the FET kinetics data. Folding was triggered by GuHCl jump from 6.0 M to 1.0 M in a CTF mixer (pH 5.0, 18 °C). For clarity, only 8 of the 112 observed decays are displayed: (*A*) unfolded in 6.0 M GuHCl; (*B*) 150 μs after the initiation of folding reaction; (*C*) 430 μs; (*D*) 1.25 ms; (*E*) 3.41 ms; (*F*) 6.50 ms; (*G*) 7.70 ms; (*H*) >30 min (native state in 1.0 M GuHCl).

21% decrease in Trp-59 integrated fluorescence intensity (Fig. 2*B*). This reduction in Trp-59 fluorescence is likely the result of a reduction in the average Trp-59–heme distance because the change is greater than can be accounted for on the basis of the change in solvent conditions. Maximum entropy analysis of the Trp-59 fluorescence decay kinetics measured 150 μs after mixing reveals very modest changes in the Tr59–heme distance distribution compared with that of the denatured protein (Fig. 3 *A* and *B*). The presence of substantial populations of extended polypeptides indicates that the protein has not undergone a large-scale collapse upon dilution of the denaturant; the first moment of the 150-μs distribution reveals a 3-Å reduction in the average Trp-59–heme distance (Fig. 4*A* and Fig. S3). These burst-phase changes are consistent with a response of the polypeptide to the change in solvent conditions upon denaturant dilution. It is clear that 150 μs after dilution of denaturant, the cyt cb_{562} ensemble is highly heterogeneous, with a considerable range of Trp-59–heme distances.

Trp-59–heme TRFET measurements at folding times between 150 μs and 12 ms allowed us to follow the evolution of the cyt cb_{562} ensemble (Fig. 3). After the modest collapse at 150 μs is a major drop in Trp-59 fluorescence intensity (Fig. 2*B*) with a rate constant of 240 s^{-1}. This value is consistent (within experimental error) with the results from our earlier stopped-flow studies in which the folding was probed by using Trp-59 fluorescence intensity and heme UV/visible absorption measurements (26). The stopped-flow burst phase corresponded to a $\approx$70% decrease of the total fluorescence intensity (26), but with the CTF mixer we resolve the entire kinetics phase.

The time dependences of the moments of the $P(r_{DA})$ distributions (see *Methods* and *SI Appendix*) enable us to characterize the time evolution of the protein ensemble. The time courses of the first and second moments of Trp-59–heme $P(r_{DA})$ can be described by single exponential functions with nearly identical rate constants (260 and 240 s^{-1}, respectively) (Fig. 4 *A* and *B* and Fig. S3). The time dependence of the $P(r_{DA})$ variance is biphasic (Fig. 4*C* and Fig. S3): a fast phase (k_{fast} = 510 s^{-1}) corresponding to a slight increase in V is followed by a slower large-amplitude reduction in V (k_{slow} = 260 s^{-1}). This behavior is precisely that expected for a folding process in which just the unfolded ($\boldsymbol{U}$) and native ($\boldsymbol{N}$) distributions are present during refolding: the moments evolve with a rate constant equal to the sum of the folding and unfolding rates ($k_{obs} = k_u + k_f$), whereas the time dependence of the variance is biexponential with rate constants equal to k_{obs} and 2 $\times$ k_{obs} (*SI Appendix*).

Discussion

Characterization of the conformational properties of the unfolded protein is a necessary precursor to any investigation of refolding kinetics. The cyt cb_{562} Trp-59–heme distance distribution under strongly denaturing conditions (6.9 M GuHCl) is poorly described by random polymer models (freely jointed chain, wormlike chain) and simple Gaussian distribution functions (Figs. S1 and S2 and *SI Appendix*). Intrachain interactions in the unfolded state produce higher populations of proteins with Trp-59 closer to the heme than expected for a random polymer. We can exclude the possibility that the misligation of His-63 to

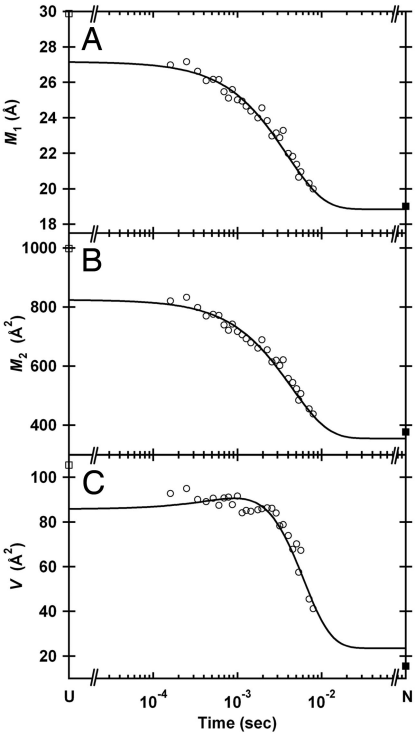

Fig. 4. Folding kinetics of cyt cb_{562} (112 original data points are logarithmically smoothed for clarity). (*A*) Mean distance between tryptophan and heme (M_1) as a function of folding time. The solid line is a fit of a single exponential function: rate constant of 2.6 ($\pm$ 0.2) $\times$ 10^2 s^{-1}. (*B*) Time course of the second moment (M_2). The solid line is a fit of a single exponential function: rate constant of 2.4 ($\pm$0.3) $\times$ 10^2 s^{-1}. (*C*) Time course of the variance (v). The solid line is a fit of a double exponential function: rate constants of 5.1 $\times$ 10^2 and 2.6 $\times$ 10^2 s^{-1}.

the heme is responsible for the population of short Trp-59–heme distances: the heme absorption spectrum is consistent with a high-spin ground state at pH 5 (26). It is interesting to compare the denatured state of cyt cb_{562} with that of the structurally similar protein cyt c'. Trp-59 of cyt cb_{562} and Trp-72 of cyt c' are located at similar sites in the four-helix bundle with nearly identical sequence separations from the heme (cyt $cb_{562,}$ 39; c', 41 residues). The Trp-72–heme distance distribution of denatured cyt c' shows a substantially larger population of extended structures, producing a greater average Trp-72–heme distance [cyt c': [GuHCl] = 3.5 M, M_1(Trp-72–heme) = 35 Å; cyt cb_{562}: [GuHCl] = 6.9 M, M_1(Trp-59–heme) = 30 Å] and a relatively small population of conformations with native-like distances (≈2%). These observations indicate that intrachain interactions in unfolded cyt cb_{562} stabilize compact structures to a greater extent than in cyt c'. The heme group has been implicated as a stabilizing element in denatured cyt b_{562}: NMR studies provide evidence for native-like conformations in cyt b_{562} in the presence of denaturants (14). Specific heme–polypeptide interactions may be responsible for the high proportion of short Trp-59–heme distances in denatured cyt cb_{562}. It is not clear, however, whether these species correspond to near-native structures.

Rapid dilution of denaturant from solutions of unfolded cyt cb_{562} initially produces only a small change in the polypeptide conformation. The Trp-59–heme distance distributions before and 150 μs after denaturant dilution are virtually identical, corresponding to just a 10% reduction in the average Trp-59–heme distance. This behavior is similar to that observed for cyt c' (29) but contrasts with results from *Saccharomyces cerevisiae* cyt *c* experiments (36, 37) where dilution of denaturant produced a substantial population (50%) of nonnative collapsed structures within 1 ms. The cyt cb_{562} TRFET data argue against a large scale collapse of the unfolded protein into a molten globule-type intermediate. Moreover, the time evolution of the Trp-59–heme distance distribution provides no evidence that significant populations of intermediate structures form during the folding process. The time dependences of M_1, M_2, and V are consistent with a model in which only denatured and fully folded polypeptide are present in significant concentrations.

Studies of wild-type and mutant forms of apo-cyt b_{562} have suggested that the protein folds according to a mechanism in which the rate-limiting step produces an intermediate that is structured in helices 2–3 and the N-terminal part of helix 4 (14, 17–22, 42). Subsequent steps involve structure formation in the remainder of helix 4, followed by folding of helix 1. Trp-59 lies near the N terminus of helix-3, close to the helix 2–3 loop. Formation of an intermediate with helices 2–3 and the N-terminal part of helix 4 in near-native conformations would bring Trp-59 substantially closer to the heme, producing the loss of fluorescence observed in the main kinetics phase. Conversion of this species into an intermediate with a fully developed C-terminal helix involves positioning the heme adjacent to helices 2 and 3, which would produce a measurable change in heme absorbance and a further reduction in Trp-59 fluorescence. The introduction of the covalently bound porphryin group at the terminus of helix 4 might have been expected to increase substantially the barrier to the second step in this sequence. In this case, we would have observed formation of an intermediate with a structure analogous to that produced by helix-destabilizing mutations in the apoprotein (18, 21, 42). Nevertheless, folding in cyt cb_{562} appears to proceed without the formation of stable intermediates, suggesting that either the presence of the heme group does not introduce a barrier larger than that for helix 2–3 formation or that the refolding mechanism of cyt cb_{562} is different from that of the apoprotein. In either case, the results point to considerable robustness in the folding of this four-helix bundle, consistent with the notions of minimal frustration (43–47). The final slow phase of cyt cb_{562} folding (5 s^{-1}) is associated primarily with changes in the heme absorption spectrum and may involve formation of the native heme coordination environment [Fe-S(Met-7)] (26). Native ferric cyt b_{562} does not fold efficiently because of heme dissociation (14, 24). Rather than disrupting the folding process, introduction of a *c*-type heme linkage in cyt cb_{562} apparently leads to more efficient delivery of the heme into the helical bundle (25, 26).

Methods

Materials. *N*-Acteyltryptophanamide (NATA), *N*-bromosuccinimide, and GuHCl Sigma Ultra grade were used as received from Sigma. Cyt cb_{562} was expressed and purified as described in ref. 26.

Experimental Conditions. The kinetic folding reactions were initiated by mixing a solution of denatured cyt cb_{562} in 6 M GuHCl [50 mM sodium acetate (NaOAc, pH 5.0)] with NaOAc buffer [50 mM (pH 5.0)] at a volume ratio of 1:5. Protein concentrations were confirmed by absorption spectroscopy (ε_{415} = 148 mM^{-1} cm^{-1}) (26), and the final concentrations of the cyt cb_{562} were 10–13 μM. All measurements were conducted at ambient temperature (≈18 °C). GuHCl concentrations were determined by refractive index measurements (48).

TRFET Experimental Configuration. The T-shaped continuous-flow mixer (40) was used to follow the folding reaction of cyt cb_{562} as described in ref. 29.

Steady-state and time-resolved Trp fluorescence-decay kinetics measurements were carried out with a picosecond streak camera (C5680; Hamamatsu Photonics) in the photon-counting (28, 49) and analog integration (29) modes, respectively. For the time-resolved measurements, weak fluorescence from the buffer solution was subtracted before data analysis. Trp fluorescence decay kinetics were measured on both short (1 ns) and long (20 ns) time scales, whose time resolutions are ≈2 and ≈40 ps, respectively.

Data Fitting and Analysis. The resulting short- and long-time scale data were spliced together, and the combined traces were compressed logarithmically before fitting (70 points per decade). We confirmed that the compression does not alter the interpretation of data.

TRFET analysis involves the numerical inversion of a Laplace transform [$I(t) = \sum_k P(k) \exp(-kt)$] (50, 51). We have used two algorithms to invert our kinetics data with regularization methods that impose additional constraints on the properties of $P(k)$. The simplest constraint that applies to the TRFET is that $P(k) \geq 0$ ($\forall\ k$). We have fit the kinetics data by using a MATLAB (Mathworks) algorithm (LSQNONNEG) that minimizes the sum of the squared deviations (χ^2) between observed and calculated values of $I(t)$, subject to a nonnegativity constraint. It is our experience that LSQNONNEG produces the narrowest $P(k)$ distributions and smallest values of χ^2 with relatively few nonzero components. Information theory suggests that the least biased solution to this inversion problem minimizes χ^2 and maximizes the breadth of $P(k)$ (52). This regularization condition can be met by maximizing the Shannon–Jaynes entropy of the rate-constant distribution {$S = -\sum_k P(k)\ln[P(k)]$}, implicitly requiring that $P(k) \geq 0$ ($\forall\ k$) (53). Maximum-entropy (ME) fitting produces stable and reproducible numerical inversions of the kinetics data. The balance between χ^2 minimization and entropy maximization is determined by graphical L curve analysis (54). This approach yields upper limits for the widths of $P(k)$ consistent with our experimental data. The $P(k)$ distributions from ME fitting are broader than those obtained with LSQNONNEG fitting but exhibit maxima in similar locations. A simple coordinate transformation using the Förster equation (Eq. 1)

$$k = k_0\left(1 + \left(\frac{r_0}{r_{\mathbf{DA}}}\right)^6\right) \qquad [1]$$

recasts the probability distribution of the decay rates, $P(k)$, obtained by LSQNONNEG or ME fitting as probability distributions over $r_{\mathbf{DA}}$ (55, 56). The Förster critical length, r_0, for the Trp-59–heme pair in cyt cb_{562}, is 34 Å under both native and unfolded conditions. The value of k_0 ($3.2 \times 10^8\ s^{-1}$) was obtained from luminescence decay measurements with NATA (10 μM) in the CTF mixer under various solvent conditions [50 mM NaOAc with and without GuHCl (0, 1.0, and 6.0 M) at pH 5.0]. At distances longer than $1.5r_0$, energy transfer quenching of **D** is not competitive with excited-state decay, and, at distances less than ≈10 Å, the Förster model does not reliably describe FET kinetics (57, 58); accordingly, our cyt cb_{562} FET kinetics measurements can provide information about **D**–**A** center-to-center distances only in the range $10 \leq r_{\mathbf{DA}} \leq 44$ Å.

The $P(r_{\mathbf{DA}})$ distributions are characterized by their moments: the first and second moments (M_n, $n = 1, 2$) (Eq. 2) correspond to the mean and mean-squared **D**–**A** distances in the ensemble; the second central moment or variance (V, Eq. 3) reflects the breadth of the distribution.

$$M_n = \langle r_{\mathbf{DA}}^n \rangle = \frac{\sum P(r_{\mathbf{DA}}) \cdot r_{\mathbf{DA}}^n}{\sum P(r_{\mathbf{DA}})} \qquad [2]$$

$$V = M_2 - (M_1)^2\,. \qquad [3]$$

ACKNOWLEDGMENTS. We thank Professor Linda Thöny-Meyer (Eidgenössische Technische Hochschule Zürich, Zürich, Switzerland) for the *ccm* plasmid pEC86. We also thank Ekaterina V. Pletneva for many helpful discussions. This work was supported by National Institutes of Health Grants GM068461 (to J.R.W.) and DK019038 (to H.B.G.) and by an Arnold and Mabel Beckman Foundation Senior Research Fellowship (to J.C.L.). T.K. was supported by Japan Society for the Promotion of Science Postdoctoral Fellowships for Young Scientists and for Research Abroad.

1. Bryngelson JD, Onuchic JN, Socci ND, Wolynes PG (1995) Funnels, pathways, and the energy landscape of protein folding: A synthesis. *Proteins* 21:167–195.
2. Dill KA, Chan HS (1997) From Levinthal to pathways to funnels. *Nat Struct Biol* 4:10–19.
3. Onuchic JN, LutheySchulten Z, Wolynes PG (1997) Theory of protein folding: The energy landscape perspective. *Annu Rev Phys Chem* 48:545–600.
4. Onuchic JN, Wolynes PG (2004) Theory of protein folding. *Curr Opin Struct Biol* 14:70–75.
5. Plotkin SS, Onuchic JN (2002) Understanding protein folding with energy landscape theory. Part I. Basic concepts. *Q Rev Biophys* 35:111–167.
6. Plotkin SS, Onuchic JN (2002) Understanding protein folding with energy landscape theory. Part II. Quantitative aspects. *Q Rev Biophys* 35:205–286.
7. Portman JJ, Takada S, Wolynes PG (2001) Microscopic theory of protein folding rates. I. Fine structure of the free energy profile and folding routes from a variational approach. *J Chem Phys* 114:5069–5081.
8. Portman JJ, Takada S, Wolynes PG (2001) Microscopic theory of protein folding rates. II. Local reaction coordinates and chain dynamics. *J Chem Phys* 114:5082–5096.
9. Wain R, et al. (2001) The cytochrome *c* fold can be attained from a compact apo state by occupancy of a nascent heme binding site. *J Biol Chem* 276:45813–45817.
10. Borgia A, Gianni S, Brunori M, Travaglini-Allocatelli C (2008) Fast folding kinetics and stabilization of apocytochrome *c*. *FEBS Lett* 582:1003–1007.
11. Moore CD, Lecomte JTJ (1990) Structural properties of apocytochrome b_5: Presence of a stable native core. *Biochemistry* 29:1984–1989.
12. Moore CD, Almisky ON, Lecomte JTJ (1991) Similarities in structure between holocytochrome b_5 and apocytochrome b_5: NMR studies of the histidine residues. *Biochemistry* 30:8357–8365.
13. Fersht AR, Matouschek A, Serrano L (1992) The folding of an enzyme. 1. Theory of protein engineering analysis of stability and pathway of protein folding. *J Mol Biol* 224:771–782.
14. Garcia P, et al. (2005) Effects of heme on the structure of the denatured state and folding kinetics of cytochrome b_{562}. *J Mol Biol* 346:331–344.
15. Fuentes EJ, Wand AJ (1998) Local stability and dynamics of apocytochrome b_{562} examined by the dependence of hydrogen exchange on hydrostatic pressure. *Biochemistry* 37:9877–9883.
16. Manyusa S, Whitford D (1999) Defining folding and unfolding reactions of apocytochrome b_5 using equilibrium and kinetic fluorescence measurements. *Biochemistry* 38:9533–9540.
17. Feng HQ, Takei J, Lipsitz R, Tjandra N, Bai YW (2003) Specific nonnative hydrophobic interactions in a hidden folding intermediate: Implications for protein folding. *Biochemistry* 42:12461–12465.
18. Feng HQ, Vu ND, Zhou Z, Bai YW (2004) Structural examination of ϕ-value analysis in protein folding. *Biochemistry* 43:14325–14331.
19. Choy WY, Zhou Z, Bai YW, Kay LE (2005) An ^{15}N NMR spin relaxation dispersion study of the folding of a pair of engineered mutants of apocytochrome b_{562}. *J Am Chem Soc* 127:5066–5072.
20. Feng H, Zhou Z, Bai Y (2005) A protein folding pathway with multiple folding intermediates at atomic resolution. *Proc Natl Acad Sci USA* 102:5026–5031.
21. Zhou Z, Huang YZ, Bai YW (2005) An on-pathway hidden intermediate and the early rate-limiting transition state of Rd-apocytochrome b_{562} characterized by protein engineering. *J Mol Biol* 352:757–764.
22. Wang T, et al. (2007) Probing the folding intermediate of Rd-apocytochrome b_{562} by protein engineering and infrared T-jump. *Protein Sci* 16:1176–1183.
23. Wang LJ, Sun N, Terzyan S, Zhang XJ, Benson DR (2006) Histidine/tryptophan π-stacking interaction stabilizes the heme-independent folding core of microsomal apocytochrome b_5 relative to that of mitochondrial apocytochrome b_5. *Biochemistry* 45:13750–13759.
24. Wittung-Stafshede P, Lee JC, Winkler JR, Gray HB (1999) cytochrome b_{562} folding triggered by electron transfer: Approaching the speed limit for formation of a four-helix bundle protein. *Proc Natl Acad Sci USA* 96:6587–6590.
25. Faraone-Mennella J, Gray HB, Winkler JR (2005) Early events in the folding of four-helix bundle heme proteins. *Proc Natl Acad Sci USA* 102:6315–6319.
26. Faraone-Mennella J, Tezcan FA, Gray HB, Winkler JR (2006) Stability and folding kinetics of structurally characterized cytochrome cb_{562}. *Biochemistry* 45:10504–10511.
27. Lee JC, Gray HB, Winkler JR (2001) cytochrome *c′* folding triggered by electron transfer: Fast and slow formation of four-helix bundles. *Proc Natl Acad Sci USA* 98:7760–7764.
28. Lee JC, Engman KC, Tezcan FA, Gray HB, Winkler JR (2002) Structural features of cytochrome *c′* folding intermediates revealed by fluorescence energy-transfer kinetics. *Proc Natl Acad Sci USA* 99:14778–14782.
29. Kimura T, Lee JC, Gray HB, Winkler JR (2007) Site-specific collapse dynamics guide the formation of the cytochrome *c′* four-helix bundle. *Proc Natl Acad Sci USA* 104:117–122.
30. Pletneva EV, et al. (2007) Probing the cytochrome *c′* folding landscape. *J Inorg Biochem* 101:1768–1775.
31. Hill EE, Morea V, Chothia C (2002) Sequence conservation in families whose members have little or no sequence similarity: The four-helical cytokines and cytochromes. *J Mol Biol* 322:205–233.
32. Shibata N, et al. (1998) Basis for monomer stabilization in *Rhodopseudomonas palustris* cytochrome *c′* derived from the crystal structure. *J Mol Biol* 284:751–760.
33. Bertini I, et al. (2004) NMR-validated structural model for oxidized *Rhodopseudomonas palustris* cytochrome c_{556}. *J Biol Inorg Chem* 9:224–230.
34. Arnesano F, et al. (2000) Structural consequences of *b*- to *c*-type heme conversion in oxidized *Escherichia coli* cytochrome b_{562}. *Biochemistry* 39:1499–1514.
35. Lyubovitsky JG, Gray HB, Winkler JR (2002) Structural features of the cytochrome *c* molten globule revealed by fluorescence energy transfer kinetics. *J Am Chem Soc* 124:14840–14841.
36. Lyubovitsky JG, Gray HB, Winkler JR (2002) Mapping the cytochrome *c* folding landscape. *J Am Chem Soc* 124:5481–5485.
37. Pletneva EV, Gray HB, Winkler JR (2005) Snapshots of cytochrome *c* folding. *Proc Natl Acad Sci USA* 102:18397–18402.
38. Pletneva EV, Gray HB, Winkler JR (2005) Nature of the cytochrome *c* molten globule. *J Am Chem Soc* 127:15370–15371.
39. Pletneva EV, Gray HB, Winkler JR (2005) Many faces of the unfolded state: Conformational heterogeneity in denatured yeast cytochrome *c*. *J Mol Biol* 345:855–867.
40. Akiyama S, et al. (2002) Conformational landscape of cytochrome *c* folding studied by microsecond-resolved small-angle X-ray scattering. *Proc Natl Acad Sci USA* 99:1329–1334.
41. Kimura T, et al. (2005) Specific collapse followed by slow hydrogen bond formation of β-sheet in the folding of single-chain monellin. *Proc Natl Acad Sci USA* 102:2748–2753.

42. ChuRA, Pei WH, Takei J, Bai YW (2002) Relationship between the native-state hydrogen exchange and folding pathways of a four-helix bundle protein. *Biochemistry* 41:7998–8003.
43. Cranz-Mileva S, Friel CT, Radford SE (2005) Helix stability and hydrophobicity in the folding mechanism of the bacterial immunity protein Im9. *Protein Eng Des Sel* 18:41–50.
44. Gsponer J, et al. (2006) Determination of an ensemble of structures representing the intermediate state of the bacterial immunity protein Im7. *Proc Natl Acad Sci USA* 103:99–104.
45. Le Duff CS, Whittaker SB, Radford SE, Moore GR (2006) Characterisation of the conformational properties of urea-unfolded Im7: Implications for the early stages of protein folding. *J Mol Biol* 364:824–835.
46. Ferreiro DU, Hegler JA, Komives EA, Wolynes PG (2007) Localizing frustration in native proteins and protein assemblies. *Proc Natl Acad Sci USA* 104:19819–19824.
47. Sutto L, Latzer J, Hegler JA, Ferreiro DU, Wolynes PG (2007) Consequences of localized frustration for the folding mechanism of the IM7 protein. *Proc Natl Acad Sci USA* 104:19825–19830.
48. Nozaki Y (1972) The preparation of guanidine hydrochloride. *Methods Enzymol* 26: 43–50.
49. Lee JC, Langen R, Hummel PA, Gray HB, Winkler JR (2004) α-Synuclein structures from fluorescence energy-transfer kinetics: Implications for the role of the protein in Parkinson's disease. *Proc Natl Acad Sci USA* 101:16466–16471.
50. Beals JM, Haas E, Krausz S, Scheraga HA (1991) Conformational studies of a peptide corresponding to a region of the C terminus of ribonuclease A: Implications as a potential chain-folding initiation site. *Biochemistry* 30:7680–7692.
51. Beechem JM, Haas E (1989) Simultaneous determination of intramolecular distance distributions and conformational dynamics by global analysis of energy transfer measurements. *Biophys J* 55:1225–1236.
52. Istratov AA, Vyvenko OF (1999) Exponential analysis in physical phenomena. *Rev Sci Instr* 70:1233–1257.
53. Livesey AK, Delaye M, Licinio P, Brochon JC (1987) Maximum-entropy analysis of dynamic parameters via the Laplace transform. *Faraday Disc* 83:247–258.
54. Lawson CL, Hanson RJ (1974) *Solving Least Squares Problems* (Prentice–Hall, Englewood Cliffs, NJ).
55. Förster T (1948) *Ann Phys* 2:55–75.
56. Wu P, Brand L (1994) Resonance energy transfer: Methods and applications. *Anal Biochem* 218:1–13.
57. Jordanides XJ, Scholes GD, Shapley WA, Reimers JR, Fleming GR (2004) Electronic couplings and energy transfer dynamics in the oxidized primary electron donor of the bacterial reaction center. *J Phys Chem B* 108:1753–1765.
58. Scholes GD, Jordanides XJ, Fleming GR (2001) Adapting the Förster theory of energy transfer for modeling dynamics in aggregated molecular assemblies. *J Phys Chem B* 105:1640–1651.